

Analysis of interphase node proteins in fission yeast by quantitative and superresolution fluorescence microscopy

Matthew Akamatsu^{a,b,c}, Yu Lin^{c,d,e}, Joerg Bewersdorf^{c,e}, and Thomas D. Pollard^{a,b,d,*}

^aDepartment of Molecular, Cellular and Developmental Biology, ^bDepartment of Molecular Biophysics and Biochemistry, ^cIntegrated Graduate Program in Physical and Engineering Biology, ^dDepartment of Cell Biology, and ^eDepartment of Biomedical Engineering, Yale University, New Haven, CT 06520-8103

ABSTRACT We used quantitative confocal microscopy and FPALM superresolution microscopy of live fission yeast to investigate the structures and assembly of two types of interphase nodes—multiprotein complexes associated with the plasma membrane that merge together and mature into the precursors of the cytokinetic contractile ring. During the long G2 phase of the cell cycle, seven different interphase node proteins maintain constant concentrations as they accumulate in proportion to cell volume. During mitosis, the total numbers of type 1 node proteins (cell cycle kinases Cdr1p, Cdr2p, Wee1p, and anillin Mid1p) are constant even when the nodes disassemble. Quantitative measurements provide strong evidence that both types of nodes have defined sizes and numbers of constituent proteins, as observed for cytokinesis nodes. Type 1 nodes assemble in two phases—a burst at the end of mitosis, followed by steady increase during interphase to double the initial number. Type 2 nodes containing Blt1p, Rho-GEF Gef2p, and kinesin Klp8p remain intact throughout the cell cycle and are constituents of the contractile ring. They are released from the contractile ring as it disassembles and then associate with type 1 nodes around the equator of the cell during interphase.

Monitoring Editor

Diane Lidke
University of New Mexico

Received: Jul 19, 2016

Revised: Apr 14, 2017

Accepted: May 15, 2017

INTRODUCTION

Fission yeast divide by cytokinesis, in which constriction of a contractile ring made of actin and myosin (Stachowiak *et al.*, 2014) and growth of the extracellular septum (Proctor *et al.*, 2012) form a furrow at the equator of the cell. The contractile ring forms from clusters of cytokinesis proteins called nodes that are associated with the plasma membrane around the middle of the cell (Vavylonis *et al.*, 2008). Cytokinesis nodes have stoichiometric proportions of constituent proteins (Wu and Pollard, 2005; Laporte *et al.*, 2011). Super-resolution measurements (Laplante *et al.*, 2016b) and two-color confocal distance measurements (Laporte *et al.*, 2011) show that

cytokinesis nodes have a regular organization, with myosin-II tails anchored to a compact base near the plasma membrane containing anillin Mid1p and myosin-II heads projecting into the cytoplasm. Mid1p serves as a scaffold for other cytokinesis proteins (Paoletti and Chang, 2000; Celton-Morizur *et al.*, 2004; Wu *et al.*, 2006; Almonacid *et al.*, 2009; Laporte *et al.*, 2011; Saha and Pollard, 2012).

During interphase, two types of nodes composed of different proteins appear in distinct regions of the cell and later merge to form cytokinesis nodes (Akamatsu *et al.*, 2014). Stationary type 1 nodes containing cell cycle kinases Cdr1p, Cdr2p, and Wee1p form around the middle of cells early during interphase and accumulate anillin Mid1p from the nucleus (Martin and Berthelot-Grosjean, 2009; Moseley *et al.*, 2009). The type 2 node proteins Blt1p, Gef2p, and Nod1p are concentrated in contractile rings and emerge as discrete, punctate structures as the ring disperses (Moseley *et al.*, 2009; Zhu *et al.*, 2013; Akamatsu *et al.*, 2014). During interphase, type 2 nodes diffuse along the cell cortex until they are captured by stationary type 1 nodes around the equator after 1.5–2 h (Akamatsu *et al.*, 2014). The combined nodes subsequently accumulate cytokinesis proteins early in mitosis (Moseley *et al.*, 2009; Saha and Pollard, 2012) to form cytokinesis nodes. Animal cells may also use node-like clusters of contractile ring proteins as precursors for

This article was published online ahead of print in MBoC in Press (<http://www.molbiolcell.org/cgi/doi/10.1091/mbc.E16-07-0522>) on May 24, 2017.

J.B. discloses a financial interest in Bruker Corp. and Hamamatsu Photonics K.K.

*Address correspondence to: Thomas D. Pollard (thomas.pollard@yale.edu).

Abbreviations used: FPALM, fluorescence photoactivation localization microscopy; mEGFP, monomeric enhanced green fluorescent protein; mEOS3.2, monomeric EOS version 3.2; SIN, septation initiation network; SPB, spindle pole body.

© 2017 Akamatsu *et al.* This article is distributed by The American Society for Cell Biology under license from the author(s). Two months after publication it is available to the public under an Attribution–Noncommercial–Share Alike 3.0 Unported Creative Commons License (<http://creativecommons.org/licenses/by-nc-sa/3.0>).

“ASCB®,” “The American Society for Cell Biology®,” and “Molecular Biology of the Cell®” are registered trademarks of The American Society for Cell Biology.

contractile rings (Straight *et al.*, 2003; Werner *et al.*, 2007; Hickson and O'Farrell, 2008; Zhou and Wang, 2008; Wollrab *et al.*, 2016; Henson *et al.*, 2017).

Previous work left open four important questions about interphase nodes. First, the wide range of fluorescence intensities of interphase nodes marked with Cdr2p, Mid1p, Gef2p, or Blt1p (Laporte *et al.*, 2011; Ye *et al.*, 2012; Zhu *et al.*, 2013; Pan *et al.*, 2014) raised the question of whether interphase nodes are defined units or might be amorphous protein aggregates. It was uncertain whether the compositions of interphase nodes are heterogeneous, whether the presence of variable numbers of unitary structures was obscured by the limited resolution of the confocal microscope, or both.

Second, the numbers of nodes during interphase was uncertain. Three studies using confocal microscopy agreed that type 1 nodes marked by Cdr2p–green fluorescent protein (GFP) double in number during interphase (Deng and Moseley, 2013; Bhatia *et al.*, 2014; Pan *et al.*, 2014). However, the reported number of type 1 nodes varied from 10–20 in a midfocal plane (Bhatia *et al.*, 2014) to 25–40 (Pan *et al.*, 2014) or ~52–106 in whole cells (Deng and Moseley, 2013).

Third, incomplete information about the cellular concentrations of interphase node proteins (especially those in type 2 nodes) left us wondering whether any of their concentrations change during the cell cycle. Quantitative confocal microscopy was used to estimate the number of interphase node proteins including Mid1p (Wu and Pollard, 2005; Coffman *et al.*, 2011; Laporte *et al.*, 2011), Gef2p and Nod1p (Zhu *et al.*, 2013), and Cdr2p (Pan *et al.*, 2014) in whole cells and interphase nodes. Mass spectrometry showed that the numbers of Cdr2p, Blt1p, and Klp8p were constant around the time of mitosis, but no measurements were made for the other ~80% of the cell cycle during interphase (Carpy *et al.*, 2014). No quantitative measurements were available for Klp8p, Cdr1p, or Wee1p.

Fourth, Blt1p, the presumed scaffold for type 2 nodes, is incorporated into contractile rings, but nodes are not resolved within rings by confocal microscopy (Moseley *et al.*, 2009; Goss *et al.*, 2014). Therefore, we did not know whether nodes remain intact or whether Blt1p disperses in contractile rings.

We used quantitative confocal microscopy and high-speed fluorescence photoactivation localization microscopy (FPALM; Huang *et al.*, 2013) of live fission yeast cells to address each of these questions. We investigated the organization and stoichiometry of proteins in interphase nodes across the cell cycle. Both types of measurements suggest that interphase nodes are unitary structures that increase in number over the cell cycle. The observations also confirmed our speculation (Akamatsu *et al.*, 2014) that type 2 nodes marked by Blt1p persist as discrete structures within the contractile ring.

RESULTS

Interphase node proteins accumulate in proportion to cell volume

We measured the total numbers per cell of seven interphase node proteins tagged with GFP or monomeric enhanced GFP (mEGFP) at the N- or C-terminus by quantitative confocal microscopy (Figure 1 and Table 1). Six of these proteins were expressed from the genome under the control of their native promoters. mEGFP-Gef2p was overexpressed due to a second promoter upstream of the resistance gene (Zhu *et al.*, 2013). These tagged strains grew normally (Supplemental Figure S1). We examined populations of asynchronous cells and used cell lengths to estimate cell cycle time.

The cellular concentrations of the four type 1 node proteins (Cdr1p, Cdr2p, Wee1p, and Mid1p) and three type 2 node proteins

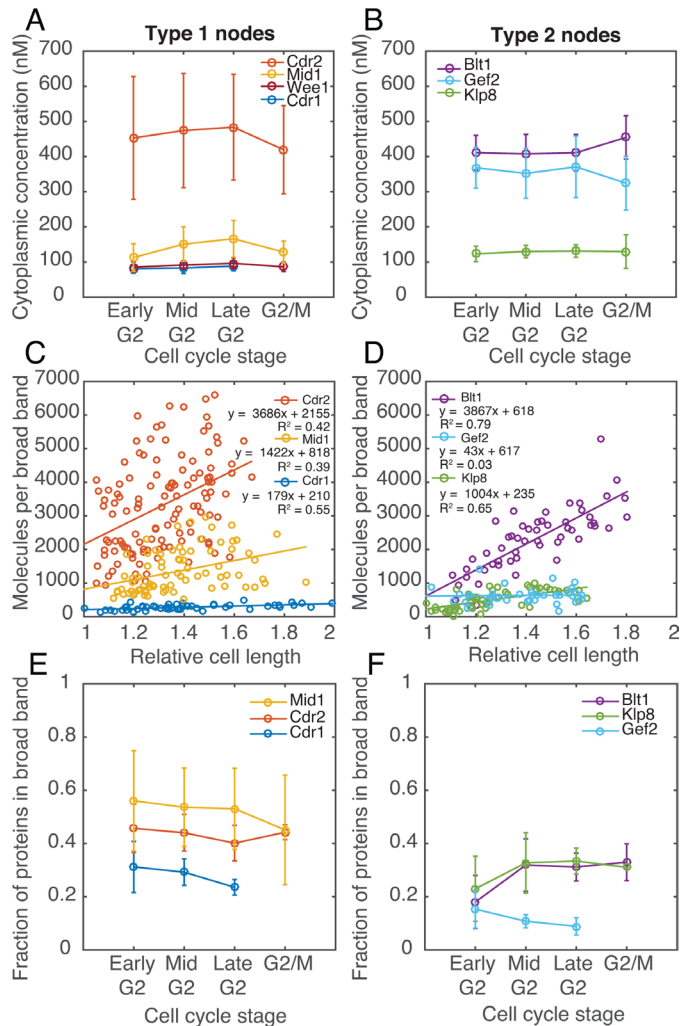


FIGURE 1: Global and local numbers of molecules of interphase node proteins over the cell cycle measured by quantitative fluorescence microscopy (see *Materials and Methods*). Values in A, B, E, and F are means \pm SD. (A, B) Concentrations of (A) type 1 and (B) type 2 interphase node proteins over the cell cycle. Cells were classified into interphase stages by cell length. (C, D) Numbers of molecules in the broad band of nodes over the cell cycle for (C) type 1 and (D) type 2 interphase node proteins. The x-axis (relative cell length) is defined as the cell length scaled relative to the smallest (1) and largest (2) cell in the population. Extrapolation of linear fits to $x = 1$ give the average number of molecules at the cell equator at cell birth. Cells expressing Cdr1p-3GFP were shorter than wild-type cells (Martin and Berthelot-Grosjean, 2009; Moseley *et al.*, 2009) and so their lengths were scaled independently. (E, F) Fractions of each interphase node protein in the broad band of nodes over the cell cycle for (E) type 1 and (F) type 2 nodes. Cells were classified into interphase stages by cell length.

(Gef2p, Blt1p, and Klp8p) were constant during the cell cycle (Figure 1, A and B), that is, their total numbers per cell increased in proportion to cell size. The scaffold proteins Cdr2p and Blt1p are present at higher concentrations than the other node proteins.

Our data confirm previous fluorescence intensity measurements on Mid1p (Wu and Pollard, 2005) using a range of calibration standards and on Cdr2p (Pan *et al.*, 2014) using the ratio of Cdr2p-GFP to Rlc1p-GFP and the concentration of Rlc1p-GFP (Wu and Pollard, 2005; Supplemental Table S1). Our numbers also agree within a factor of two with measurements by mass spectrometry of Cdr2p,

| Protein | Molecules per cell | Cellular concentration (nM) | Molecules per broad band | Molecules per ring | Estimated molecules per node ^a |
|---------|--------------------|-----------------------------|--------------------------|--------------------|---|
| Cdr1 | 1000 ± 350 (55) | 83 ± 14 | 280 ± 92 (49) | n/a | ~2–3 |
| Wee1 | 2100 ± 620 (51) | 89 ± 14 | n.d. | n/a | n.d. |
| Cdr2 | 7900 ± 3100 (155) | 460 ± 160 | 3300 ± 1400 (122) | ~500 | ~30 |
| Mid1 | 2700 ± 1100 (95) | 140 ± 46 | 1400 ± 640 (77) | 1000 ± 230 (6) | ~10 |
| Gef2 | 6400 ± 1900 (48) | 360 ± 77 | 650 ± 280 (38) | 880 ± 230 (5) | n.d. |
| Klp8 | 2000 ± 660 (44) | 130 ± 23 | 480 ± 300 (53) | 650 ± 220 (9) | ~5 |
| Blt1 | 8400 ± 2200 (76) | 420 ± 59 | 2100 ± 820 (56) | 3000 ± 490 (15) | ~20 |

Measurements of molecules in the contractile ring were made for fully formed (continuous) unconstricting rings. Values ± SD, with number of cells measured in parentheses. n.d., not determined; n/a, not applicable.

^aNumber of molecules per broad band of nodes divided by the number of nodes.

TABLE 1: Measurement by quantitative confocal fluorescence microscopy of number of molecules of interphase node proteins per cell, in the broad band, and per node.

Blt1p, and Klp8p during the G2–S interval of the cell cycle (Carpy *et al.*, 2014). That study did not report the numbers of these node proteins for the vast majority of interphase, ~80% of the cell cycle, and the time of interest for our study. Carpy *et al.* (2014) examined cells arrested at G2/M for 5 h, which produced a heterogeneous population of abnormally large cells. They divided all of their numbers by 3.5, an estimate of the average difference in size of their cell population and wild-type cells. They and Zhu *et al.* (2013) reported ~2000 Gef2p molecules at the end of G2, so Gef2p was overexpressed by ~3.5-fold in our cells. Other counts of cytokinesis proteins by mass spectrometry (Marguerat *et al.*, 2012) differ from fluorescence measurements even by more than an order of magnitude (Coffman and Wu, 2014; Supplemental Table S1).

Interphase node proteins accumulate around the equator during interphase

Owing to their accumulation in nodes, the total numbers of type 1 node proteins increased linearly in the broad band around the equator during interphase (Figure 1, C and D). These measurements are consistent with previous qualitative observations (Deng and Moseley, 2013; Pan *et al.*, 2014). Type 1 nodes form around the equator before cell separation (Paoletti and Chang, 2000; Morrell *et al.*, 2004; Martin and Berthelot-Grosjean, 2009; Moseley *et al.*, 2009; Akamatsu *et al.*, 2014), and so the numbers of type 1 node proteins in the broad band are already high in short early G2 cells. Linear regression fits to the counts of molecules versus cell length allowed us to determine the mean number of molecules in the broad band of nodes (*y*-intercepts) in early interphase: ~2200 Cdr2p, ~800 Mid1p, and 200 Cdr1p. The numbers of all three proteins approximately doubled during interphase (Figure 1C) before Cdr2p and

Cdr1p dispersed from nodes during mitosis. When expressed at endogenous concentrations, the kinase GFP-Wee1p was present in interphase nodes (Supplemental Figure S2B), but the low signal and its presence at the spindle pole body (SPB) precluded accurate measurements of its number in the equatorial broad band. The fraction of each type 1 node protein in the broad band of nodes remained relatively constant throughout interphase (30–50% of the total cellular pool; Figure 1E).

Type 2 nodes began the cell cycle concentrated at the new poles created by cytokinesis (Moseley *et al.*, 2009; Saha and Pollard, 2012; Akamatsu *et al.*, 2014; Goss *et al.*, 2014), and their numbers around the equator were low. During interphase, type 2 nodes moved to the cell equator (Akamatsu *et al.*, 2014), where the total numbers of Blt1p and Klp8p increased fourfold to fivefold (Figure 1D). From early G2 to mid G2, the fraction of Blt1p and Klp8p located in the broad band of nodes increased from 20 to 30% (*p* < 0.01; Figure 1F). Once type 1 and 2 nodes merged around the equator (Akamatsu *et al.*, 2014), the ratios of their constituent proteins in nodes remained fairly constant (Table 2). Overexpressed mEGFP-Gef2p did not increase around the equator during interphase, most likely because most of the signal was in the cytoplasm and was included in the measurements of the broad band.

We calculated the ratios of molecules in the broad band during late interphase relative to the least abundant protein measured, 1 Cdr1p: ~12 Cdr2p, 5 Mid1p, 2 Klp8p, and 8 Blt1p (Table 1). These ratios changed little between mid G2 and G2/M (Table 2).

Number of proteins in interphase nodes is quantized

We used quantitative confocal microscopy to measure the fluorescence intensities of individual nodes of interphase fission yeast cells

| Protein | Early G2 | Mid G2 | Late G2 | G2/M | Late interphase |
|---------|----------------|---------------|--------------|-------------|-----------------|
| Cdr1 | 1 (21) | 1 (19) | 1 (9) | n.d. | 1 |
| Cdr2 | 14 ± 6 (44) | 12.5 ± 5 (44) | 12 ± 5 (32) | 12 ± 2 (2) | 12 |
| Mid1 | 4.5 ± 6 (17) | 5 ± 2 (36) | 5.5 ± 2 (17) | 3.5 ± 2 (8) | 5 |
| Gef2 | 4 ± 2.5 (7) | 2 ± 0.5 (14) | 2 ± 0.5 (17) | n.d. | n.d. |
| Klp8 | 1.5 ± 0.5 (27) | 2 ± 0.5 (14) | 2 ± 0.5 (12) | 1 ± 0 (1) | 2 |
| Blt1 | 5 ± 2.5 (10) | 8 ± 2 (17) | 8 ± 2 (17) | 8 ± 2 (10) | 8 |

Values ± SD, with number of cells measured in parentheses. n.d., not determined.

TABLE 2: Ratios of numbers of molecules per node at different stages of interphase relative to the least abundant protein measured (Cdr1p).

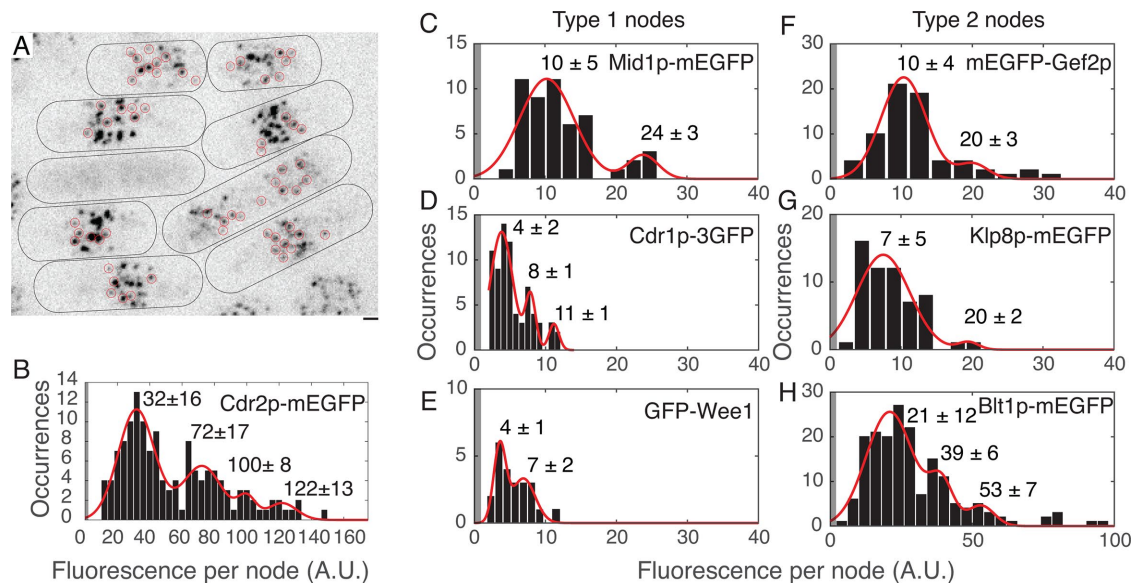


FIGURE 2: Fluorescence intensities of individual type 1 and 2 interphase nodes. (A) Field of cells expressing Cdr2p-mEGFP. Reverse contrast fluorescence micrograph of a sum projection of five slices closest to the coverslip. Red circles are node regions selected for fluorescence measurements (see *Materials and Methods*). Black lines outline cells. Scale bar, 1 μ m. (B–H) Histograms of fluorescence intensity per node. The continuous curves are fits of multiple Gaussian distributions to the data. Peak values are means \pm SD from the fits. Shaded regions on the left of each graph is background fluorescence intensity plus 1 SD. (B) $n = 138$ spots in 33 cells; (C) 23 spots in 4 cells; (D) 72 spots in 20 cells; (E) 23 spots in 11 cells; (F) 68 spots in 18 cells; (G) 58 spots in 17 cells; and (H) 177 spots in 29 cells.

expressing one of seven interphase node proteins tagged with mEGFP at the N- or C-terminus (Supplemental Table S2). We collected z-series of confocal images and measured the fluorescence intensities in five confocal slices separated by 260 nm (Figure 2A). The fluorescence intensities of individual interphase nodes were stable during 2.5 min of observation at intervals of 1 or 2 s after correcting for the overall photobleaching of the cells (Supplemental Figure S3). The two presumed scaffold proteins, Cdr2p and Blt1p, are the most abundant proteins in the two types of nodes.

Both type 1 and 2 interphase nodes varied widely in fluorescence intensity and size in the confocal microscope (Figure 2A; Coffman *et al.*, 2011; Laporte *et al.*, 2011; Ye *et al.*, 2012; Zhu *et al.*, 2013; Pan *et al.*, 2014). The large, bright, heterogeneous nodes attracted the eye, but most nodes had low intensities and uniform sizes. We used two strategies to measure fluorescence intensity in these nodes. The analysis in Figure 2 was restricted to small nodes that were well separated from other nodes and with their fluorescence included entirely in five z-sections. We measured the fluorescence in regions 7 pixels (\sim 583 nm) in diameter encircling these small nodes.

Histograms of the fluorescence intensities of the interphase node proteins revealed peaks corresponding to multiples of a unitary value (Figure 2, B–H). Nodes with the unitary fluorescence were the most numerous. For example, in the sampled population of nodes marked with Cdr2p, 57% were unitary, 28% were binary, and the remainder had higher fluorescence intensities. Thus some nodes are located so close together that we count them as one node with a multiple of the unitary fluorescence. These fluorescence intensity histograms were better fitted by multiple Gaussian distributions (Figure 2) than by continuous log-normal distributions (Supplemental Figure S2, H–N, and Supplemental Table S3). In cells coexpressing Cdr2p-mCherry and Cdr1p-3GFP, the fluorescence intensities per node were correlated in the two channels (Supplemental Figure S2, F and G).

The foregoing analysis excluded the brightest nodes, which represented at least half of the total nodes. Using larger regions of interest to examine a sample of bright nodes that were well separated from each other, we found that their fluorescence intensities were up to 10 times the unitary fluorescence (Supplemental Figure S2, A and C–E). The fluorescence per unitary node did not change as a function of cell length (Supplemental Figure S4; Pan *et al.*, 2014).

We conclude that nodes are discrete structures with stoichiometric ratios of proteins, but many nodes are too close together to be resolved by confocal microscopy even during interphase. Therefore we turned to superresolution microscopy to test this hypothesis.

Superresolution microscopy of interphase nodes

We used the photoconvertible fluorescent protein monomeric EOS version 3.2 (mEOS3.2; Zhang *et al.*, 2012) to tag the C-termini of Cdr2p and Blt1p in the genome, so the native promoter controlled the expression of the fusion proteins. Both strains grew normally (Supplemental Figure S1). We acquired FPALM images of these cells at 200 frames/s using laser intensities that photoconverted, imaged, and bleached most of the tagged proteins in a field within 50 s (Huang *et al.*, 2013; Laplante *et al.*, 2016a; Supplemental Figure S5). The localization precision was \sim 35 nm (Supplemental Figure S5C). We imaged nodes from two perspectives—either by focusing in the middle of the cell to obtain side views of nodes along the sides of cells (Figures 3, A–C, and 4, A, B, E, and F) or by focusing on the cell surface to obtain face views (Figures 3, D–G, and 4, D and F–I).

High-speed FPALM of cells expressing tagged interphase node proteins showed that both Cdr2p-mEOS3.2 and Blt1p-mEOS3.2 concentrated in discrete structures <100 nm in diameter (Figures 3, A–C, and 4, A, B, E, and F). The following sections trace the life histories, numbers, locations, and surface densities of interphase nodes throughout the cell cycle.

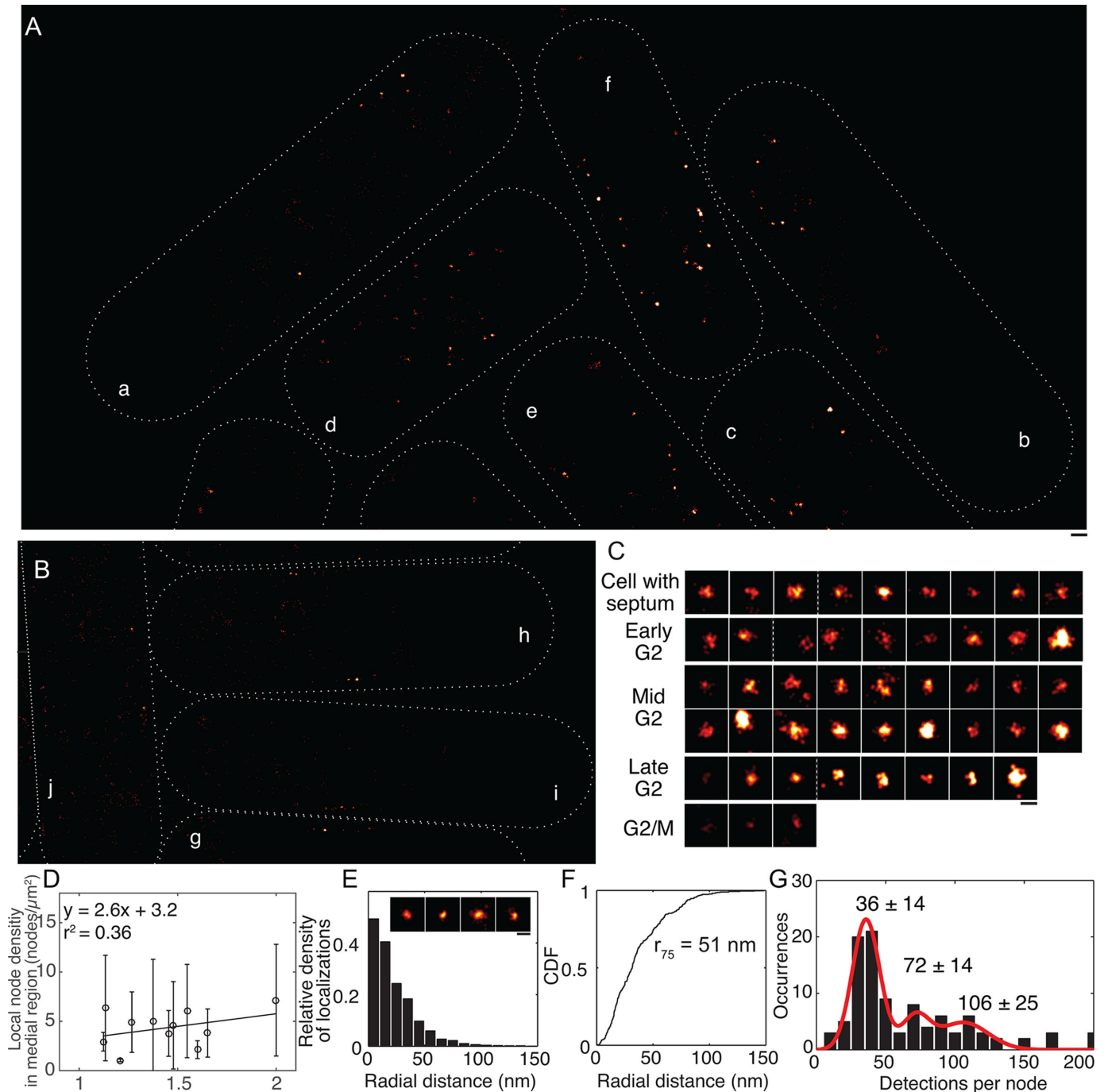


FIGURE 3: High-speed FPALM of cells expressing Cdr2p-mEOS3.2. (A, B) Gaussian kernel density heat maps in focal planes partway between a medial longitudinal section and the cell surface, which captures nodes near the surface. Cells are labeled a–i in the order of cell cycle stage based on length and the presence of a septum: a, b, cells with septa; c, d, early G2; e, f, mid G2; g, late G2; h, G2/M; and i, mitosis. White lines mark cell perimeters. Bar, 400 nm. (C) Individual nodes of cells marked in A and B with lower contrast. See *Materials and Methods* for details on cell classification. Dashed white lines separate nodes from different cells. Bar, 100 nm. (D) Surface densities of interphase nodes in a zone 1.6 μm wide centered on the equator across the cell cycle. Densities were determined by Voronoi tessellation (see Supplemental Figure S6). The sample was 122 nodes in 11 cells in three fields. Line is a linear fit. (E, F) Analysis of the spatial distribution of Cdr2p-mEOS3.2 in face views of nodes with <55 detections (approximately the $n = 1$ peak in G). (E) Histograms of the radial density distribution of mEOS3.2 detections from the center of each node. Inset, Gaussian kernel density heat maps of detections in individual nodes (face views). Bar, 100 nm. (F) Cumulative distribution plots of radial density of detections in nodes marked by Cdr2p-mEOS3.2. The 75th percentile of detection radial distances is reported. CDF, cumulative distribution function. (G) Histogram of the numbers of FPALM detections per node for face view of Cdr2p-mEOS3.2 nodes. The continuous curves are fits of multiple Gaussian distributions to the data with the peak numbers of detections indicated. Values reported are means \pm SD from the fits. $n = 92$ spots.

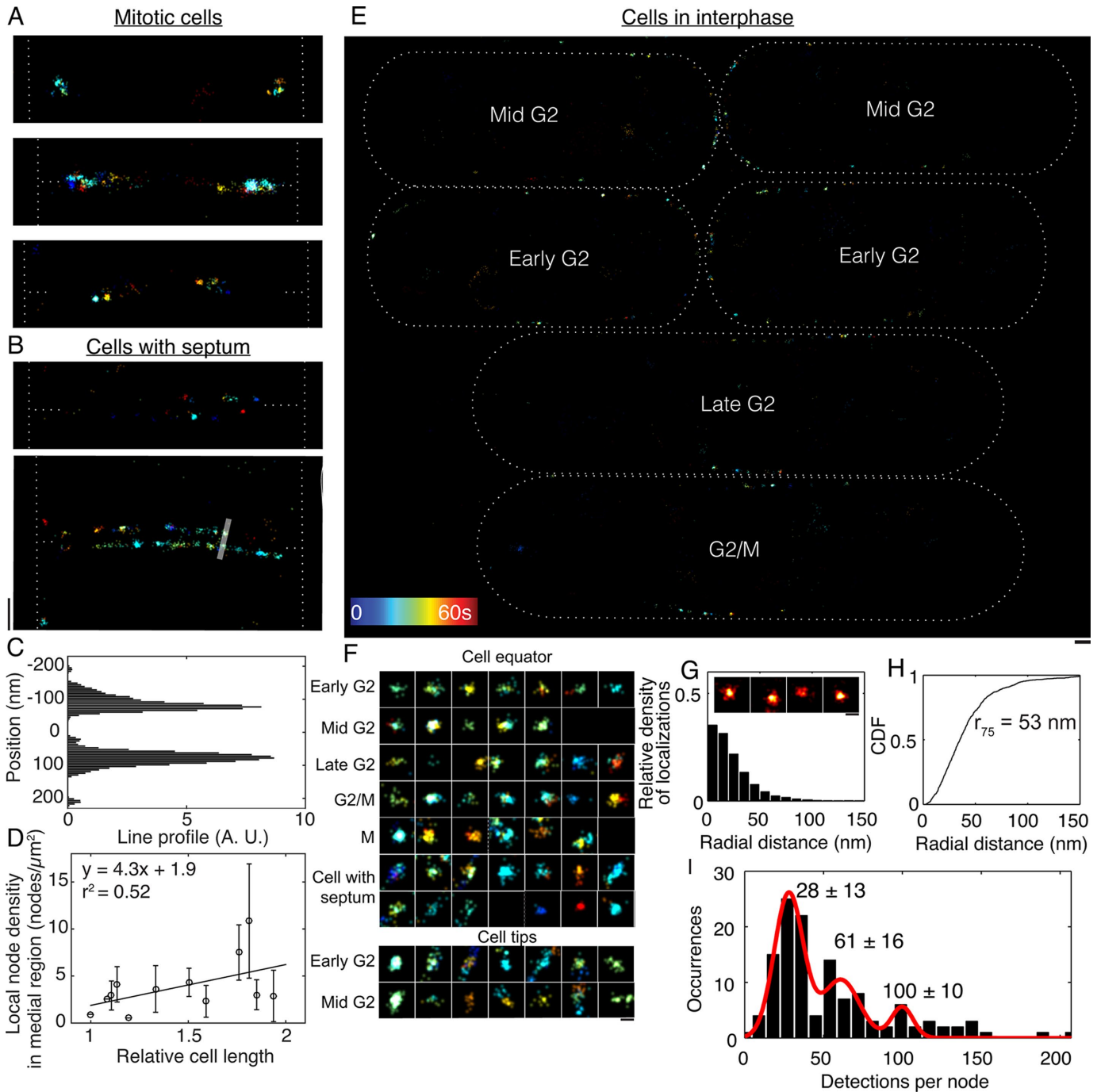


FIGURE 4: High-speed FPALM of cells expressing Blt1p-mEOS3.2. A, B, E, and F are displayed as Gaussian kernel time-colored maps according to the times when detections occurred during acquisition. Dotted white lines mark cell perimeters and sites of division. (A) Nodes in cells with contractile rings but no septum. (B) Nodes in cells with septa. Bar, 400 nm. (C) Line scan of two nodes marked in the bottom of B. Intensity values (proportional to density of detections) were averaged across the 20-pixel width of the line. (D) Local surface densities of interphase nodes in a zone 1.6 μm wide centered on the equator across the cell cycle from a sample of 472 nodes in 13 cells in two fields. Line is a linear fit. (E) Image of six interphase cells marked with cell cycle stage. Bar, 400 nm. (F) Images of individual nodes from A, B, and E arranged by cell cycle stage and location at cell equators or cell tips. Dashed white lines separate nodes from different cells. Bar, 100 nm. (G, H) Analysis of the spatial distribution of Blt1p-mEOS3.2 in face views of nodes with <50 detections (approximately the $n = 1$ peak in I). (G) Histograms of the radial density distribution of detections from the center of each node. Inset, Gaussian kernel density heat maps of detections in individual nodes (face views). Bar, 100 nm. (H) Cumulative distribution plots of the radial density of detections in nodes marked by Blt1p-mEOS3.2. CDF, cumulative distribution function. The 75th percentile of detection radial distances is reported. (I) Histogram of the numbers of FPALM detections per node for face views of nodes. The continuous curves are fits of multiple Gaussian distributions to the data with the peak numbers of detections indicated. Values reported are means \pm SD from the fits. $n = 125$ spots.

Superresolution microscopy of type 1 interphase nodes

After being dispersed in the cytoplasm during mitosis (Figures 2A and 3Bj), Cdr2p-mEOS3.2 reappeared in discrete, punctate structures <100 nm in diameter on the inside of the plasma membrane around the nuclei of both daughter cells (Figure 3A, a and b). Throughout interphase, Cdr2p-mEOS3.2 remained localized to these discrete structures distributed in a broad band around the cell equator. These images of type 1 nodes were sharp because type 1 nodes have low diffusion coefficients (Akamatsu *et al.*, 2014) and moved less than the precision of the imaging method during the time of acquisition. These punctate structures appeared similar in side views (Figure 3, A–C) and face views (Figure 3E). The appearance of Cdr2p-mEOS3.2 in these new nodes was indistinguishable from that in type 1 nodes later during interphase, so we did not detect any intermediate forms.

The numbers of localized detections of Cdr2p per node covered a wide range but clustered in discrete peaks corresponding to multiples of a unitary number of 36 detections per node (Figure 3G), similar to our confocal microscopy observations (Supplemental Figure S4I and Supplemental Table S3). In the sampled population of nodes marked with Cdr2p (all discrete spots with Gaussian distributions of detections), 58% were unitary, 17% were binary, and the remainder had higher numbers of detections. Thus many nodes were located so close to neighbors that they were not resolved even by superresolution microscopy. The numbers of localized detections per node did not change as a function of cell length (Supplemental Figure S4H).

We assessed the spatial distribution of Cdr2p-mEOS3.2 detections within nodes with unitary numbers of detections (<55 detections per node) by measuring the radial distance of each detection from the center of mass of the node. The numbers of detections declined radially from the center, with 75% within 51 nm of the center (Figure 3F). All of these unitary nodes were similar in size (Supplemental Figure S4, J–M).

The local densities (Supplemental Figure S6) of nodes imaged around the equator by FPALM varied from cell to cell but increased modestly during interphase (Figure 3D). This is consistent with previous measurements by confocal microscopy, which showed that the numbers of nodes (Deng and Moseley, 2013; Pan *et al.*, 2014) increased during interphase faster than the increase in the width of the broad band of nodes (Bhatia *et al.*, 2014; Pan *et al.*, 2014).

Superresolution microscopy of type 2 interphase nodes

Blt1p-mEOS3.2 appeared in discrete, punctate structures <100 nm in diameter near the plasma membrane throughout the cell cycle (Figure 4, A and E). The appearance of these nodes was similar in side views (Figure 4, A, B, E, and F) and face views (Figure 4G). However, clusters of detections of Blt1p-mEOS3.2 in type 2 nodes were larger near the cell poles than around the equator (Figure 4F). Temporal color coding showed that some clusters of Blt1p-mEOS3.2 moved on a scale of hundreds of nanometers during data acquisition, giving rise to streaks or rainbow colors. Such motions are expected from the high diffusion coefficients of type 2 nodes at the tips of cells (Akamatsu *et al.*, 2014).

FPALM showed for the first time that Blt1p forms discrete structures in contractile rings during cytokinesis (Figure 4A). These clusters of Blt1p-mEOS3.2 in contractile rings were sometimes blurred but were generally indistinguishable in size and shape from interphase type 2 nodes (Figure 4, A and E). These Blt1p nodes are spaced too closely in contractile rings to be resolved by confocal microscopy.

Once a dividing cell had constricted its contractile ring and formed a septum in the cleavage furrow, Blt1p-mEOS3.2 remained

in two parallel disks of discrete, punctate structures spread along the plasma membrane forming the cleavage furrow (Figure 4B and Supplemental Figure S5H). These arrays of type 2 nodes were separated by ~155 nm (Figure 4C), corresponding to the thickness of the septum (Johnson *et al.*, 1973; Cortés *et al.*, 2012), a distance well within the precision of the FPALM measurement (Supplemental Figure S5C). These data confirm that type 2 nodes emerge from the disassembling contractile ring (Akamatsu *et al.*, 2014) and associate with the newly expanded plasma membrane lining the cleavage furrow.

After the two daughter cells separated, type 2 nodes could be observed as discrete structures at the new cell poles formed by cytokinesis and also spread along the sides of the cells (Figure 4E). These nodes were blurred in the FPALM images (Figure 4F) because diffusion coefficients ranged from 10's to ~1800 nm²/s (Akamatsu *et al.*, 2014).

During interphase, the type 2 node markers accumulated around the equator in discrete structures <100 nm in diameter, indistinguishable from interphase nodes elsewhere in the cell. Thus the number of type 2 nodes per unit area around the equator increased more than threefold (Figure 4D). The positions of each of these objects varied little over the course of 1 min of imaging, which leads to the conclusion that type 2 nodes around the equator were relatively stationary. This behavior is consistent with them being colocalized with and anchored by type 1 nodes at the equator during late interphase (Akamatsu *et al.*, 2014).

Similar to Cdr2p-mEOS3.2 in type 1 nodes, the numbers of detections of Blt1p-mEOS3.2 per node covered a wide range but distributed into multiples of a unitary number of 28 localizations per node (Figures 4I, Supplemental Figure S4I, and Supplemental Table S3). Fifty-four percent of type 2 nodes marked with Blt1p were unitary, 26% were binary, and the remainder had more detections. Radial density distributions of the numbers of detections fell off with distance from the center, with 75% of the detections appearing within 53 nm of the centers (Figure 4, G and H).

We conclude that both type 1 and type 2 nodes are discrete structures with defined sizes and numbers of constituent proteins. Whereas type 1 node proteins cycle between a diffuse cytoplasmic pool (during mitosis) and cortical nodes (during interphase), type 2 nodes remain intact throughout the cell cycle.

DISCUSSION

Our quantitative measurements by confocal microscopy and FPALM support our hypothesis that both types of nodes have defined sizes and numbers of constituent proteins. These unitary type 1 and 2 nodes are relatively uniform over the cell cycle in terms of dimensions and appearance (measured by fluorescence intensity or numbers of detections; Supplemental Figure S4). Nodes appear heterogeneous by confocal microscopy because unitary nodes cannot be resolved in local clusters of two or more nodes.

Numbers of nodes

Three groups measured the numbers of interphase nodes by confocal microscopy. Pan *et al.* (2014) reported that Cdr2p-GFP nodes increased in number from 25 to 40, an acknowledged underestimate. Bhatia *et al.* (2014) studied the midfocal plane during interphase, in which the number of nodes marked with Cdr2-GFP doubled from 10 to 20, but they did not report the total number of nodes. Deng and Moseley (2013) collected the most extensive measurements of the number of Cdr2p nodes, which increased linearly from ~52 to 106 as cells grew longer during interphase. Our estimates are similar.

We used Deng's counts of nodes versus cell length (Deng, personal communication) to calculate the numbers of unitary nodes. Our FPALM observations show that the wide range of intensities of Cdr2p nodes in confocal micrographs comes from many confocal spots containing multiple unitary nodes (Figure 2, A and B). About 57% of confocal "nodes" are unitary, 28% have two unitary nodes, and 15% have three or more unitary nodes. Given these ratios, the number of unitary type 1 nodes is ~80 in early G2 and ~160 at the end of interphase. This number of unitary type 1 nodes at the end of interphase is similar to the ~140 unitary cytokinesis nodes that Laplante *et al.* (2016b) measured by FPALM, given that 75–80% of type 1 nodes associate with type 2 nodes (Akamatsu *et al.*, 2014) and presumably mature to cytokinesis nodes.

Compositions of interphase nodes

We used this new estimate of node numbers and our measurements of the numbers of molecules in a broad band of nodes to calculate (see *Materials and Methods*) the approximate numbers of molecules in unitary interphase nodes at the end of G2 phase (Table 1). Like cytokinesis nodes (Laplante *et al.*, 2016b), mature type 1 nodes each have ~10 molecules of Mid1p. Our estimates of 10 Mid1p molecules and 30 Cdr2p molecules per node are lower than previous measurements of Cdr2p (Pan *et al.*, 2014) and Mid1p (Laporte *et al.*, 2011) by confocal microscopy because the diffraction-limited spots in those studies were not always unitary nodes. Isolated Blt1p forms tetramers (Goss *et al.*, 2014), and so the 5 Blt1p tetramers may each associate with single copies of Klp8p. Gef2p and Nod1p are also present in stoichiometric ratios (Zhu *et al.*, 2013).

Cdr2p and Blt1p are the leading candidates to be the core proteins of type 1 and 2 interphase nodes. They are the most abundant proteins in their respective nodes and are required for other node proteins to assemble (Almonacid *et al.*, 2009; Martin and Berthelot-Grosjean, 2009; Moseley *et al.*, 2009).

Both types of interphase nodes are closely associated with the plasma membrane. Multiple candidates are available to link interphase nodes to plasma membrane lipids: in type 1 nodes, Cdr2p has a C-terminal KA1 domain (Moravcevic *et al.*, 2010; Rincon *et al.*, 2014) and Mid1p has both PH and C2 domains (Celton-Morizur *et al.*, 2004; Sun *et al.*, 2015), and Blt1p in type 2 nodes binds phospholipids (Guzman-Vendrell *et al.*, 2013).

Life cycle of type 1 nodes

The numbers of each interphase node protein are constant during mitosis (Carpy, 2014), but during interphase, each accumulates in proportion to cell volume. In parallel, the numbers of molecules of type 1 node proteins increase around the middle of the cell due to an increase in the number of nodes, as the numbers of molecules per node (proportional to intensity or number of detections) do not change over the cell cycle (Supplemental Figure S4; Bhatia *et al.*, 2014; Pan *et al.*, 2014).

Therefore the biochemical state of the cell rather than gene expression controls the assembly of nodes. For example, type 1 node proteins cycle between a diffuse cytoplasmic pool (during mitosis) and cortical nodes (during interphase). The septation initiation network (SIN) signaling pathway disperses type 1 node proteins into the cytoplasm during mitosis (Morrell *et al.*, 2004; Martin and Berthelot-Grosjean, 2009; Moseley *et al.*, 2009; Akamatsu *et al.*, 2014; Pu *et al.*, 2015; Supplemental Figure S3), and the decline of SIN activity allows type 1 nodes to reassemble around the equators of the daughter cells at the end of mitosis (Pu *et al.*, 2015). The proteins recycle because Cdr2p nodes remain in cells treated with the protein synthesis inhibitor cyclohexamide (Pan *et al.*, 2014).

We find that type 1 nodes assemble in two phases: a burst at the end of mitosis assembles about half of these nodes, followed by steady increase in numbers during interphase to double the initial number. Type 1 nodes appear quickly at the end of the eclipse phase (Figure 3), either assembling on the plasma membrane or forming in the cytoplasm before binding to the plasma membrane. Pan and Chang (2014) proposed that type 1 nodes grow by accretion of smaller Cdr2p assemblies moving along the inner surface of the plasma membrane. Such small, fast-moving units cannot be detected by live-cell FPALM because they generate too few single-molecule detections.

Mid1p accumulates in type 1 nodes, which then mature by merging with type 2 nodes before accumulating cytokinesis proteins. Thus the mechanisms concentrating stationary type 1 nodes around the equator determine the distribution of type 2 nodes and site of the cleavage furrow. Mid1p comes along as a passenger on type 1 nodes rather than determining their location. In addition, Mid1p has an uncharacterized influence on the location of cytokinesis nodes because they are not confined to the equator in *mid1Δ* cells (Daga and Chang, 2005; Wu *et al.*, 2006; Almonacid *et al.*, 2009; Laporte *et al.*, 2011; Lee and Wu, 2012; Saha and Pollard, 2012).

Life cycle of type 2 nodes

Type 2 nodes remain intact throughout the cell cycle, including time in the contractile ring. Confocal microscopy established that Blt1p is associated with cytokinesis structures across the entire cell cycle, including interphase nodes, cytokinesis nodes, and the contractile ring (Moseley *et al.*, 2009; Akamatsu *et al.*, 2014; Goss *et al.*, 2014). However, the discrete node structure is lost to view during mitosis, when the fluorescence in confocal images is spread uniformly throughout the contractile ring. This raised a question about the organization of Blt1p in the contractile ring. The 10-fold improvement in resolution provided by FPALM has provided a clear answer.

Blt1p remains in compact foci the size of interphase nodes within the contractile ring. The shape and size of these Blt1p loci are similar to those of cytokinesis nodes in contractile rings (Laplante *et al.*, 2016b). As the ring constricts and disassembles, Blt1p nodes remain along the cleavage furrow and can be resolved by FPALM (Figure 4 and Supplemental Figure S5). Once the nodes spread away from the division site they can again be resolved by confocal microscopy.

Formation of cytokinesis nodes

Cytokinesis nodes form by a series of reactions. First, diffusing type 2 nodes encounter and merge with stationary type 1 nodes, which establish the location of cleavage, as shown by mutations that alter the distribution of type 2 nodes (Celton-Morizur *et al.*, 2006; Padte *et al.*, 2006; Moseley *et al.*, 2009; Lee and Wu, 2012). The unitary nature of interphase nodes suggests that cytokinesis nodes form by docking of fully formed type 1 and type 2 nodes, a hypothesis for testing by further experimentation. Less likely, type 2 node proteins may add to type 1 nodes by accretion, as observed for Myo2 adding to cytokinesis nodes (Vavylonis *et al.*, 2008). The ~35-nm resolution of our FPALM images did not allow us to test this docking hypothesis or resolve any substructure.

Second, Mid1p transfers from type 1 to type 2 nodes before the type 1 node proteins disperse during mitosis (Morrell *et al.*, 2004; Martin and Berthelot-Grosjean, 2009; Moseley *et al.*, 2009; Saha and Pollard, 2012; Guzman-Vendrell *et al.*, 2013; Jourdain *et al.*, 2013; Zhu *et al.*, 2013; Akamatsu *et al.*, 2014; Goss *et al.*, 2014). Gef2p and binding partner Nod1p likely aid in the transfer, as Gef2p

immunoprecipitates with Mid1p and the three proteins reside stoichiometrically in nodes (Ye *et al.*, 2012; Guzman-Vendrell *et al.*, 2013; Zhu *et al.*, 2013). Then cytokinetic nodes slowly accumulate other cytokinesis proteins, resulting in ratios of one Mid1p molecule for each myosin-II Myo2 dimer, F-BAR protein Cdc15p dimer, and IQGAP Rng2p dimer (Wu and Pollard, 2005; Laporte *et al.*, 2011; Laplante *et al.*, 2016b). Based on the total numbers of these molecules around the equator and the numbers of unitary nodes counted by FPALM, cytokinesis nodes have ~10 copies of these units. Finally, forces produced by myosin on actin filaments condense cytokinesis nodes into the contractile ring (Vavylonis *et al.*, 2008).

Type 2 nodes containing Blt1p are platforms for assembly of cytokinesis nodes and ultimately the contractile ring. They are the only component of the contractile ring that remains intact throughout the cell cycle, so it is remarkable that cells lacking Blt1p are nearly normal, with only modest delays in the constriction of the contractile ring (Moseley *et al.*, 2009; Zhu *et al.*, 2013; Goss *et al.*, 2014). This indicates that cells have a reliable mechanism to back up the connections that Blt1p normally makes between proteins and the plasma membrane. For example, if mutations *cdr2Δ* or *blt1Δ* disrupt the mechanisms that normally target proteins to interphase nodes, the F-BAR protein Cdc15p slowly recruits node proteins, including Gef2p and Nod1p, to the contractile ring around or after the time of SPB separation (Ye *et al.*, 2012; Zhu *et al.*, 2013). This interdependence of redundant pathways explains the strong negative genetic interaction between mutations of *cdc15* and *blt1* (Goss *et al.*, 2014). Type 2 interphase node proteins may be some of many proteins that recruit and retain Mid1p, perhaps in relationship to its phosphorylation status during mitosis.

Fits of our histograms of fluorescence intensity or FPALM detections per node suggest that interphase nodes are discrete macromolecular assemblies (quantized distributions) rather than amorphous aggregates of proteins (continuous log-normal distributions; Supplemental Figures S2, H–N, and S5, I–J, and Supplemental Table S3). A unitary structure for nodes is consistent with the stoichiometric ratios of proteins in nodes (Supplemental Figure S2G and Table 1; Coffman *et al.*, 2011; Laporte *et al.*, 2011; Zhu *et al.*, 2013), the narrow distribution of node sizes (Figures 3E and 4H; Laplante *et al.*, 2016b), and defined positions of proteins within nodes (Laporte *et al.*, 2011; Laplante *et al.*, 2016b). This architectural information serves as the foundation for mechanistic studies of the internal organization of interphase nodes and their functions in cytokinesis.

MATERIALS AND METHODS

Strain construction

We created strains of *Schizosaccharomyces pombe* with genetically encoded fluorescent proteins using standard PCR-based gene-targeting methods (Bähler *et al.*, 1998; Laplante *et al.*, 2016a) and plasmids PFA6a-mEGFP-kanMX6 PFA6a-3GFP and pFA6a-mEos3.2-kanMX6 to insert genes for fluorescent protein mEGFP 3GFP or mEOS3.2 upstream or downstream of the open reading frame in the endogenous chromosomal locus (Supplemental Table S2). We constructed the other strains by genetic crosses to laboratory stock strains.

Some fluorescent fusion proteins were not fully functional in cells. *cdr1-3GFP* cells were shorter than wild-type cells (Martin and Berthelot-Grosjean, 2009; Moseley *et al.*, 2009; Akamatsu *et al.*, 2014), and *GFP-wee1* cells were longer than wild-type cells (Moseley *et al.*, 2009; Supplemental Figure S1B). The additional promoter in the kanMX6 cassette increased the cellular expression of N-terminally labeled mEGFP-Gef2 by approximately three to four times (Zhu *et al.*, 2013). The addition of mEOS3.2 to the C-terminus of Cdr2p or Blt1p did not affect cell growth (Supplemental Figure S1B).

Confocal microscopy

We imaged cells on gelatin pads in growth chambers containing EMM5S medium and 100 μ M *n*-propyl gallate at 25°C. We used an inverted microscope (Olympus, IX-71) with a 100 \times /1.4 numerical aperture Plan Apochromat objective (Olympus) fitted with a spinning-disk confocal head (CSU-X1; Yokogawa Corporation of America), electron-multiplying charge-coupled device camera (iXon 897; Andor Technology), argon-ion lasers (Melles Griot), acousto-optical tunable filters (Gooch and Housego), and dichroic mirrors and filters (Semrock). Images were acquired using Andor IQ2 software.

For still images, we took z-series of twenty-one 260-nm confocal slices encompassing 5.2 μ m, which covered the entire cell. For time-lapse imaging, we took z-series of three 400-nm confocal slices closest to the coverslip at 1- or 2-s intervals for ~200 s.

Data analysis

Image correction. We corrected for uneven illumination and camera offset in the confocal micrographs by imaging slides of purified monomeric yellow fluorescent protein and using automated image correction software (McCormick *et al.*, 2013). We corrected for uneven illumination in three dimensions, which also corrects for the ~40% difference in fluorescence intensity between the top and the bottom of the 3.5- μ m-diameter cells due to spherical aberrations, the difference in refractive index between the coverslip and sample. After correction, the fluorescence intensity per node was similar in nodes at the top and bottom of the cell.

We wrote custom image analysis software in ImageJ64 and MATLAB (R2015a) to semiautomatically make measurements and perform calculations on the confocal stacks of images using user-defined regions of interest. ImageJ software was written using JEdit (1.0), and some functions were adapted from published software (McCormick *et al.*, 2013; Akamatsu *et al.*, 2014).

We corrected the final fluorescence intensity values based on the fluorescent protein used: mEGFP is 1.1 times brighter than GFP (Coffman *et al.*, 2011) and 3 \times GFP is three times brighter than GFP (Wu and Pollard, 2005).

For the high-copy number calibration strain *fim1-mEGFP*, we reduced the electron multiplication (EM) gain from 300 to 100 to maintain the camera intensity values within the linear range, and scaled the resultant values accordingly. The EM gain was linear up to a value of 300.

Analysis of asynchronous cells. We used cell length as a proxy for cell cycle time (Baumgärtner and Tolic-Nørrelykke, 2009; Akamatsu *et al.*, 2014). We subdivided the 4–5 h of interphase into five stages based cell on morphology or length: early G2 cells were <8.5 μ m long, mid G2 cells were 8.5–10.5 μ m long, late G2 cells were 10.6–12.5 μ m long, and G2/M cells were >12.5 μ m long. Cdr1p-3GFP cells are shorter than wild-type cells (Martin and Berthelot-Grosjean, 2009; Moseley *et al.*, 2009), and so we defined these stages as for wild type minus 1.5 μ m (Akamatsu *et al.*, 2014). Wee1p-GFP and GFP-Wee1p cells are longer than wild type cells, so we define these stages as for wild type plus 5.5 μ m. For Figures 1, 3, and 4, we report the relative length of cells, defined as the difference ratio between current cell length and shortest cell in the population divided by the difference between the longest and shortest cells in the population. The values range from 1 at cell birth to 2 during mitosis. The y-intercept of these plots at $x = 1$ provides a measure of the mean number of molecules in the region of interest at cell birth. We scaled the length values for Cdr1p-3GFP cells independently because their mean length differs from that of wild-type cells.

Calculating cellular concentrations. We counted molecules using a calibration curve that related fluorescence intensity to number of molecules based on quantitative immunoblots (Wu and Pollard, 2005; McCormick et al., 2013). This calibration method agrees with orthogonal methods of measuring molecules within ~30% (Coffman et al., 2011; Lawrimore et al., 2011; McCormick et al., 2013). We circled cells manually and measured the fluorescence summed over all 21 260-nm slices. From the cellular regions, we extracted the cell length (Feret's diameter, defined as the longest distance between two points in the region), area, and sum fluorescence intensity for analysis. We estimated the cytoplasmic volume for each cell based on its area, the average area of the cells measured, and the assumption that the average fission yeast cell cytoplasm has a volume of 27 μm^3 (Wu and Pollard, 2005). These concentration measurements are the total number of molecules per cell divided by the scaled estimate of cellular volume.

Calculating the number of molecules per region. We measured the fluorescence in a region the width of the cell and containing >95% of the fluorescence of the object of interest: 1 μm wide for the contractile ring and 4 μm wide for the equatorial band of nodes. To account for cytoplasmic and cellular background, we measured fluorescence from a region containing the original measurement region that was two times greater in area or the length of the cell if twice the original region exceeded the cell length (Wu et al., 2008). For cells in early interphase with nodes near the cell tips, this background measurement did not cover the nodes concentrated at the new cell tip but sometimes included other nodes scattered outside the broad band of nodes. We could not measure the number of molecules of Wee1p per broad band due to the low signal of GFP-Wee1p in nodes relative to background and its localization to the spindle pole body. The fraction of proteins in broad band (Figure 1, E and F) is defined as the number of molecules per broad band divided by the number of molecules per cell on a per-cell basis. We used a two-sample Kolmogorov–Smirnov test to evaluate the significance of the increase in the fraction of molecules per broad band between early and mid G2 (Figure 1F).

Calculating fluorescence intensity per node. We measured the fluorescence intensity per node as the sum of fluorescence intensity in five consecutive 260-nm confocal slices closest to the coverslip. We made measurements of nodes containing fluorescence in at least three consecutive slices that did not have fluorescence in the adjacent slices outside the five-slice stack. We measured background fluorescence intensity from cytoplasmic regions in the cell (Sirotkin et al., 2010; Coffman and Wu, 2012). For Supplemental Figure S2, C–E, we measured the total fluorescence within continuous regions corresponding to a node or a clump of nodes, as depicted in Supplemental Figure S2A. This included regions that contained additional fluorescence outside the five-slice stack used for quantification. For Supplemental Figure S2, F and G, we compared the fluorescence intensity of nodes marked by Cdr2p-mCherry and Cdr1p-3xGFP in the same cell. We generated regions of interest surrounding diffraction-limited spots that contained the fluorescence of nodes in each channel. We report the intensity in each channel subtracted by the mean cytoplasmic background fluorescence in the field. To generate the background fluorescence measurements in Figure 2, we measured the fluorescence intensity for each background region of interest, subtracted by all the other background regions in that cell. We plot the mean \pm SD of this background fluorescence value.

Fitting Gaussian distributions to histograms. We used the MATLAB curve-fitting tool to fit each histogram in Figures 2, 3G, and 4I

using a nonlinear least squares method. We used equations for the sum of three or four Gaussian distributions. We set the amplitudes, SDs, and means for each of the Gaussian distributions as free parameters, with constraints that the parameters be positive. We set parameter starting values for the fit as integers within the order of magnitude observed for each distribution.

Comparison of fit quality. We calculated the *F* statistic to compare the quality of the fits between multiple Gaussian distributions and a log-normal distribution for each histogram in Figures 2, 3G, and 4I (Supplemental Figures S2 and S4 and Supplemental Table S3). The *F* statistic is the ratio of the sum of squared errors between the two fits normalized by the number of degrees of freedom (where a higher *F* value corresponds to a better fit for the first model).

Analysis of time-lapse images. To analyze time-lapse fluorescence images of nodes, we used a simplified version of software that tracks actin patches (Berro and Pollard, 2014). Regions were selected manually, automatically recentered at each time point with a custom algorithm using a Gaussian kernel (Berro and Pollard, 2014), and then plotted with custom MATLAB software.

For nodes that changed in fluorescence intensity over the course of imaging, we checked that the maximum fluorescence stayed in the middle slice for the duration of the imaging. We measured the background fluorescence over time from 10–20 peripheral regions containing no discrete fluorescence. We averaged the fluorescence measurements over time and between regions within a cell to generate a background measurement for each cell. The value of the background varied by 6–8% in regions within the cell (coefficient of variation 0.05–0.08) and varied by 5% between cells in an asynchronous population. We previously used these time-lapse images to report the diffusion coefficients of nodes using their positions over time (Akamatsu et al., 2014), but we did not report their fluorescence intensities over time.

Analysis of node number and estimate of molecules per node. We used raw unbinned data from Deng and Moseley (2013) to calculate the number of unitary type 1 nodes. Their measurements of type 1 node number by confocal microscopy are the most reliable and agree with our estimates by FPALM, using average surface density measurements and assumptions about the surface area of the broad band of nodes. We used their linear regression to estimate that the measured number of nodes increased from 52 (7.5- μm cells) to 106 (14.8- μm cells). We used the ratios of unitary versus multiple nodes from Figure 2A to convert this number to the number of unitary nodes. We divided our measurements of the numbers of molecules per broad band by these measurements of node number to estimate the numbers of molecules per node.

FPALM

We imaged cells on gelatin pads in growth chambers containing EMM5S and 100 μM *n*-propyl gallate at 25°C. We imaged cells with a custom-built single-molecule switching microscope (Laplante et al., 2016a) with the following modifications: fluorescence emission from mEos3.2 was collected by the objective and separated from the excitation light by a dichroic mirror (FF01-408/504/581/667/762; Semrock) and a bandpass filter (ET605/70; Chroma) before being focused onto the sensor chip of the scientific complementary metal-oxide semiconductor (sCMOS) camera.

FPALM acquisition. We illuminated the cells with 3–8 kW/cm^2 from the 561-nm laser for 10 s before acquisition to bleach

autofluorescence and mEOS3.2 that had been photoconverted before the beginning of the experiment. In most experiments, we increased the intensity of the 405-nm photoconversion laser from 0 to 38 W/cm² in a series of even steps every 5 or 15 s. To minimize premature photoactivation and bleaching, we found the correct focal plane by bright-field microscopy. We focused on the middle of a field of cells in bright field to image cells in a longitudinal section ~400 nm thick. To image the surface of cells closest to the coverslip, we imaged regions 1.6 μ m closer to the coverslip than the medial section.

Software used to construct superresolution images

We performed data analysis and superresolution image reconstruction using sCMOS-specific single-molecule localization algorithms (Huang *et al.*, 2013). Briefly, we first corrected the raw data frames for the camera offset and gain. After single-molecule identification from the calibrated images, we cropped images of the molecules (7 \times 7 pixels) and used maximum-likelihood estimation of two-dimensional (2D) Gaussian fits to obtain the position, photon number, and background information. We used a rejection algorithm based on the log-likelihood ratio metric to remove non-convergent fits or overlapping fluorescence signals from multiple emitters. Localization uncertainty estimates were determined using Cramér–Rao lower bound with the sCMOS likelihood function. To reconstruct super-resolution images, we binned the localization estimates into 2D histogram images with 5.15 \times 5.15 nm pixel size. To aid visualization, each resulting image was convolved with a 2D Gaussian kernel with $\sigma = 1.5$ pixels.

Analysis of reconstructed FPALM nodes

Calculating local density of nodes. We generated Voronoi diagrams (also called Voronoi tessellations) to calculate the local density of nodes from FPALM images of cells. We used ImageJ to manually select all discrete spots in the image with regions of interest 231 nm in diameter and record the spots' x- and y-positions within each cell. We wrote a MATLAB program to record the position of each node, length of the cell, and its long-axis angle relative to the x-axis. The program retained nodes with ≥ 14 detections for further analysis. The program calls the function "voronoin.m" to generate a Voronoi diagram for all of the nodes in each cell. The Voronoi diagram partitions the cell surface into polygons each containing one node. For a given node and its polygon, each point on the polygon is closer to that node than to any other node. The area of each polygon is the inverse of the local density of that node. To account for overlapping nodes, we divided the area of the polygon by integer values corresponding to the number of unitary nodes as determined from the numbers of detections (Figures 3G and 4I). To account for cell edges, the boundary was periodic and rotated according to the cell axis angle.

For the plots in Figures 3D and 4F, we calculated the mean node density for the middle 1.8 μ m of the cell's length for consistency with confocal measurements. The slopes and r^2 values in these figures were similar if the middle region was 4 μ m long.

Calculating number of detections per node and radial distance.

We manually selected all discrete regions in 50-s reconstructions of FPALM images and saved the regions for analysis using the algorithms described in Laplante (2016a). Briefly, for each region, we made 2D histograms of the detections within the region with a pixel size of 2 nm and identified the radial symmetry center (Parthasarathy, 2012) of each region. We fitted radially symmetric 2D Gaussian distributions to each FPALM node using a maximum-

likelihood method and retained nodes for further analysis based on the quality of the fit.

For nodes retained after the foregoing filtering step, we measured the numbers of detections per region and report these values as histograms in Figures 3 and 4. We fitted three Gaussian distributions as explained for the histograms of fluorescence per node to identify the number of detections corresponding to unitary, double, or triple nodes.

For nodes within the unitary number of detections (≤ 55 detections for Cdr2p or ≤ 50 detections for Blt1p), we measured the distance of each detection from the node center (obtained by the Gaussian fit) and report histograms of the radial distances, with each distance bin normalized by the value of the radius. We plot the cumulative distributions of these histograms and report the radial distance that contains at least 75% of localizations, as well as the full-width at half-maximum, defined as two times the 50th percentile of radial distances. These two measurements are not directly comparable because each radial distance bin occupies a different amount of area.

ACKNOWLEDGMENTS

We thank Jian-Qiu Wu and Hirohisa Masuda for providing strains, Chad McCormick and Julien Berro for ImageJ macros, Thomas Fai for help creating Voronoi diagrams, Charlotte Kaplan for advice on FPALM localization distribution analysis, and Fang Huang for FPALM reconstruction and analysis software. This work was supported by National Institutes of Health Research Grants GM-026132 and GM-026338 and Grant 095927/A/11/Z from the Wellcome Trust.

REFERENCES

- Akamatsu M, Berro J, Pu K-M, Tebbs IR, Pollard TD (2014). Cytokinetic nodes in fission yeast arise from two distinct types of nodes that merge during interphase. *J Cell Biol* 204, 977–988.
- Almonacid M, Moseley JB, Janvore J, Mayeux A, Fraisier V, Nurse P, Paoletti A (2009). Spatial control of cytokinesis by Cdr2 kinase and Mid1/anillin nuclear export. *Curr Biol* 19, 961–966.
- Bähler J, Wu JQ, Longtine MS, Shah NG, McKenzie A, Steever AB, Wach A, Philippsen P, Pringle JR (1998). Heterologous modules for efficient and versatile PCR-based gene targeting in *Schizosaccharomyces pombe*. *Yeast* 14, 943–951.
- Baumgärtner S, Tolic-Nørrelykke IM (2009). Growth pattern of single fission yeast cells is bilinear and depends on temperature and DNA synthesis. *Biophys J* 96, 4336–4347.
- Berro J, Pollard TD (2014). Local and global analysis of endocytic patch dynamics in fission yeast using a new "temporal superresolution" realignment method. *Mol Biol Cell* 25, 3501–3514.
- Bhatia P, Hachet O, Hersch M, Rincon SA, Berthelot-Grosjean M, Dalessi S, Basterra L, Bergmann S, Paoletti A, Martin SG (2014). Distinct levels in Pom1 gradients limit Cdr2 activity and localization to time and position division. *Cell Cycle* 13, 538–552.
- Carpy A, Krug K, Graf S, Koch A, Popic S, Hauf S, Macek B (2014). Absolute proteome and phosphoproteome dynamics during the cell cycle of *Schizosaccharomyces pombe* (fission yeast). *Mol Cell Proteomics* 13, 1925–1936.
- Celton-Morizur S, Bordes N, Fraisier V, Tran PT, Paoletti A (2004). C-terminal anchoring of mid1p to membranes stabilizes cytokinetic ring position in early mitosis in fission yeast. *Mol Cell Biol* 24, 10621–10635.
- Celton-Morizur S, Racine V, Sibarita J-B, Paoletti A (2006). Pom1 kinase links division plane position to cell polarity by regulating Mid1p cortical distribution. *J Cell Sci* 119, 4710–4718.
- Coffman VC, Wu J-Q (2012). Counting protein molecules using quantitative fluorescence microscopy. *Trends Biochem Sci* 37, 499–506.
- Coffman VC, Wu JQ (2014). Every laboratory with a fluorescence microscope should consider counting molecules. *Mol Biol Cell* 25, 1545–1548.
- Coffman VC, Wu P, Parthun MR, Wu JQ (2011). CENP-A exceeds microtubule attachment sites in centromere clusters of both budding and fission yeast. *J Cell Biol* 195, 563–572.

- Cortés JCG, Sato M, Muñoz J, Moreno MB, Clemente-Ramos JA, Ramos M, Okada H, Osumi M, Durán A, Ribas JC (2012). Fission yeast Ags1 confers the essential septum strength needed for safe gradual cell abscission. *J Cell Biol* 198, 637–656.
- Daga RR, Chang F (2005). Dynamic positioning of the fission yeast cell division plane. *Proc Natl Acad Sci USA* 102, 8228–8232.
- Deng L, Moseley JB (2013). Compartmentalized nodes control mitotic entry signaling in fission yeast. *Mol Biol Cell* 24, 1872–1881.
- Goss JW, Kim S, Bledsoe H, Pollard TD (2014). Characterization of the roles of Blt1p in fission yeast cytokinesis. *Mol Biol Cell* 25, 1946–1957.
- Guzman-Vendrell M, Baldissar S, Almonacid M, Mayeux A, Paoletti A, Moseley JB (2013). Blt1 and Mid1 provide overlapping membrane anchors to position the division plane in fission yeast. *Mol Cell Biol* 33, 418–428.
- Henson JH, Ditzler CE, Germain A (2017). The ultrastructural organization of actin and myosin II filaments in the contractile ring: new support for an old model of cytokinesis. *Mol Biol Cell* 28, 613–623.
- Hickson GRX, O'Farrell PH (2008). Rho-dependent control of anillin behavior during cytokinesis. *J Cell Biol* 180, 285–294.
- Huang F, Hartwich TMP, Rivera-Molina FE, Lin Y, Duim WC, Long JJ, Uchil PD, Myers JR, Baird MA, Mothes W, et al. (2013). Video-rate nanoscopy using sCMOS camera-specific single-molecule localization algorithms. *Nat Methods* 10, 653–658.
- Johnson BF, Yoo BY, Calleja GB (1973). Cell division in yeasts: movement of organelles associated with cell plate growth of *Schizosaccharomyces pombe*. *J Bacteriol* 115, 358–366.
- Jourdain I, Brzezińska EA, Toda T (2013). Fission Yeast Nod1 is a component of cortical nodes involved in cell size control and division site placement. *PLoS One* 8, e54142.
- Laplante C, Huang F, Bewersdorf J, Pollard TD (2016a). High-speed super-resolution imaging of live fission yeast cells. *Methods Mol Biol* 1369, 45–57.
- Laplante C, Huang F, Tebbs IR, Bewersdorf J, Pollard TD (2016b). Molecular organization of cytokinesis nodes and contractile rings by super-resolution fluorescence microscopy of live fission yeast. *Proc Natl Acad Sci USA* 113, E5876–E5885.
- Laporte D, Coffman VC, Lee I-J, Wu J-Q (2011). Assembly and architecture of precursor nodes during fission yeast cytokinesis. *J Cell Biol* 192, 1005–1021.
- Lawrimore J, Bloom KS, Salmon ED (2011). Point centromeres contain more than a single centromere-specific Cse4 (CENP-A) nucleosome. *J Cell Biol* 195, 573–582.
- Lee I-J, Wu J-Q (2012). Characterization of Mid1 domains for targeting and scaffolding in fission yeast cytokinesis. *J Cell Sci* 125, 2973–2985.
- Marguerat S, Schmidt A, Codlin S, Chen W, Aebersold R, Bähler J (2012). Quantitative analysis of fission yeast transcriptomes and proteomes in proliferating and quiescent cells. *Cell* 151, 671–683.
- Martin SG, Berthelot-Grosjean M (2009). Polar gradients of the DYRK-family kinase Pom1 couple cell length with the cell cycle. *Nature* 459, 852–856.
- McCormick CD, Akamatsu MS, Ti S-C, Pollard TD (2013). Measuring affinities of fission yeast spindle pole body proteins in live cells across the cell cycle. *Biophys J* 105, 1324–1335.
- Moravcevic K, Mendrola JM, Schmitz KR, Wang Y-H, Slochower D, Janmey PA, Lemmon MA (2010). Kinase associated-1 domains drive MARK/PAR1 kinases to membrane targets by binding acidic phospholipids. *Cell* 143, 966–977.
- Morrell JL, Nichols CB, Gould KL (2004). The GIN4 family kinase, Cdr2p, acts independently of septins in fission yeast. *J Cell Sci* 117, 5293–5302.
- Moseley JB, Mayeux A, Paoletti A, Nurse P (2009). A spatial gradient coordinates cell size and mitotic entry in fission yeast. *Nature* 459, 857–860.
- Padte NN, Martin SG, Howard M, Chang F (2006). The cell-end factor pom1p inhibits mid1p in specification of the cell division plane in fission yeast. *Curr Biol* 16, 2480–2487.
- Pan KZ, Saunders TE, Flor-Parra I, Howard M, Chang F (2014). Cortical regulation of cell size by a sizer cdr2p. *Elife* 3, e02040.
- Paoletti A, Chang F (2000). Analysis of mid1p, a protein required for placement of the cell division site, reveals a link between the nucleus and the cell surface in fission yeast. *Mol Biol Cell* 11, 2757–2773.
- Parthasarathy R (2012). Rapid, accurate particle tracking by calculation of radial symmetry centers. *Nat Methods* 9, 724–726.
- Proctor SA, Minc N, Boudaoud A, Chang F (2012). Contributions of turgor pressure, the contractile ring, and septum assembly to forces in cytokinesis in fission yeast. *Curr Biol* 22, 1601–1608.
- Pu K-M, Akamatsu M, Pollard TD (2015). The septation initiation network controls the assembly of nodes containing Cdr2p for cytokinesis in fission yeast. *J Cell Sci* 128, 441–446.
- Rincon SA, Bhatia P, Bicho C, Guzman-Vendrell M, Fraiser V, Borek WE, Alves F de L, Dingli F, Loew D, Rappalber J, et al. (2014). Pom1 regulates the assembly of Cdr2-Mid1 cortical nodes for robust spatial control of cytokinesis. *J Cell Biol* 206, 61–77.
- Saha S, Pollard TD (2012). Anillin-related protein Mid1p coordinates the assembly of the cytokinetic contractile ring in fission yeast. *Mol Biol Cell* 23, 3982–3992.
- Sirotkin V, Berro J, Macmillan K, Zhao L, Pollard TD (2010). Quantitative analysis of the mechanism of endocytic actin patch assembly and disassembly in fission yeast. *Mol Biol Cell* 21, 2894–2904.
- Stachowiak MR, Laplante C, Chin HF, Guirao B, Karatekin E, Pollard TD, O'Shaughnessy B (2014). Mechanism of cytokinetic contractile ring constriction in fission yeast. *Dev Cell* 29, 547–561.
- Straight AF, Cheung A, Limouze J, Chen I, Westwood NJ, Sellers JR, Mitchison TJ (2003). Dissecting temporal and spatial control of cytokinesis with a myosin II inhibitor. *Science* 299, 1743–1747.
- Sun L, Guan R, Lee I-J, Liu Y, Chen M, Wang J, Wu J-Q, Chen Z (2015). Mechanistic insights into the anchorage of the contractile ring by anillin and Mid1. *Dev Cell* 33, 413–426.
- Vavylonis D, Wu JQ, Hao S, O'Shaughnessy B, Pollard TD (2008). Assembly mechanism of the contractile ring for cytokinesis by fission yeast. *Science* 319, 97–100.
- Werner M, Munro E, Glotzer M (2007). Astral signals spatially bias cortical myosin recruitment to break symmetry and promote cytokinesis. *Curr Biol* 17, 1286–1297.
- Wollrab V, Thiagarajan R, Wald A, Kruse K, Riveline D (2016). Still and rotating myosin clusters determine cytokinetic ring constriction. *Nat Commun* 7, 1–9.
- Wu J-Q, McCormick CD, Pollard TD (2008). Chapter 9: counting proteins in living cells by quantitative fluorescence microscopy with internal standards. *Methods Cell Biol* 89, 253–273.
- Wu J-Q, Pollard TD (2005). Counting cytokinesis proteins globally and locally in fission yeast. *Science* 310, 310–314.
- Wu J-Q, Sirotkin V, Kovar DR, Lord M, Beltzner CC, Kuhn JR, Pollard TD (2006). Assembly of the cytokinetic contractile ring from a broad band of nodes in fission yeast. *J Cell Biol* 174, 391–402.
- Ye Y, Lee I-J, Runge KW, Wu J-Q (2012). Roles of putative Rho-GEF Gef2 in division-site positioning and contractile-ring function in fission yeast cytokinesis. *Mol Biol Cell* 23, 1181–1195.
- Zhang M, Chang H, Zhang Y, Yu J, Wu L, Ji W, Chen J, Liu B, Lu J, Liu Y, et al. (2012). Rational design of true monomeric and bright photoactivatable fluorescent proteins. *Nat Methods* 9, 727–729.
- Zhou M, Wang Y-L (2008). Distinct pathways for the early recruitment of myosin II and actin to the cytokinetic furrow. *Mol Biol Cell* 19, 318–326.
- Zhu YH, Ye Y, Wu Z, Wu JQ (2013). Cooperation between Rho-GEF Gef2 and its binding partner Nod1 in the regulation of fission yeast cytokinesis. *Mol Biol Cell* 24, 3187–3204.